Granular decoherence precedes ice mélange failure and glacier calving at Jakobshavn Isbræ

Ryan K. Cassotto [1] ✉, Justin C. Burton [2], Jason M. Amundson [3], Mark A. Fahnestock[4] and Martin Truffer[4]

The stability of the world's largest glaciers and ice sheets depends on mechanical and thermodynamic processes occurring at the glacier–ocean boundary. A buoyant agglomeration of icebergs and sea ice, referred to as ice mélange, often forms along this boundary and has been postulated to affect ice-sheet mass losses by inhibiting iceberg calving. Here, we use terrestrial radar data sampled every 3 min to show that calving events at Jakobshavn Isbræ, Greenland, are preceded by a loss of flow coherence in the proglacial ice mélange by up to an hour, wherein individual icebergs flowing in unison undergo random displacements. A particle dynamics model indicates that these fluctuations are likely due to buckling and rearrangements of the quasi-two-dimensional material. Our results directly implicate ice mélange as a mechanical inhibitor of iceberg calving and further demonstrate the potential for real-time detection of failure in other geophysical granular materials.

ce mélange is a granular material composed of iceberg 'grains'[1] up to 1,000 m or more in length that can affect tidewater glacier systems through a variety of feedbacks. It can source considerable amounts of cold freshwater into fjords[2,3] and exert drag on underlying waters[4,5], potentially affecting fjord heat transport[6] and submarine melting of glacier ice. Moreover, ice mélange can affect mass losses from glacier termini by mechanically resisting the calving of large icebergs[7,8] associated with glacial earthquakes[9–12], thereby providing opportunities to assess the evolution of mechanical failure in geophysical systems.

When densely packed in a fjord, ice mélange forms a disordered, jammed state[13–15] where icebergs flow in unison. Between calving events, ice mélange velocities are consistent with laboratory experiments and numerical simulations of quasi-two-dimensional (2D) granular materials that are pushed through straight channels[16–18]. These experiments exhibit heterogeneous viscoplastic flow with deformation concentrated in shear zones near the channel walls, and uniform, plug flow in the middle of the channels. However, this flow is sensitive to external stress. Calving events inject large amounts of energy into the head of a fjord, producing a dynamic jamming front[19] that propagates through the kilometres-long ice mélange ~20 times faster than the speed of individual icebergs[20]. Typically, grain-scale information must be acquired at sufficient spatial and temporal resolution to quantify the rheological properties of granular materials[21–24]. However, such detailed information rarely exists in complex geophysical systems.

In this study, we exploit recent developments in terrestrial radar interferometry (TRI) to observe grain-scale ice mélange dynamics before and after calving events. We use a pair of TRIs to generate 2D flow fields and strain rates along the proglacial ice mélange of Jakobshavn Isbræ, Greenland's most prolific iceberg-producing glacier[25]. The record reveals an evolution of ice mélange rheology from coherent iceberg flow during periods of terminus quiescence to decoherent flow associated with random displacements of individual icebergs beginning 1 h before calving. An accompanying particle dynamics model demonstrates that a small downfjord expansion of the ice mélange facilitates these displacements. Our results provide the best evidence yet that ice mélange can control the timing of iceberg calving, with implications for tidewater glacier retreat and ice mass loss from the major ice sheets.

Observing and characterizing modes of ice mélange flow

Jakobshavn Isbræ is one of Greenland's fastest flowing outlet glaciers. A perennial ice mélange occupies the inner fjord, stretching >10 km from the glacier's calving face with a mean thickness of ~100 m (refs. [8,18]). Previous studies[7], including one recent TRI study[26], showed that ice mélange weakening in spring precedes calving at Jakobshavn Isbræ, a phenomenon facilitated by the seasonal loss of binding sea ice[17]. Until now, no study has resolved whether ice mélange motion has preceded calving in the summer when sea ice is minimal. In this Article, we present observations from August 2012, an usually warm period in Greenland[27]. We scanned the glacier and proglacial fjord every 3 min for 10 days using a pair of Gamma Remote Sensing ground portable radar interferometers (herein referred to as TRIs). The radars were positioned ~1.9 km apart on bedrock and had substantially overlapping viewing geometries (coloured polygons in Fig. 1). Earlier results used particle image velocimetry on the radar backscatter data to examine the dynamic jamming that occurs during calving events, which produces an areal increase in ice mélange extent and causes icebergs to accelerate by three orders of magnitude[20] to >1 m s^{-1}, a quantity too fast to be quantified with the TRI's electromagnetic phase measurements. In this study, we applied the methods of Voytenko et al.[28] to the electromagnetic phase measurements from both radars to produce 2D velocity and strain rate fields to quantify the spatiotemporal evolution of the ice mélange prior to and following several iceberg calving events[29]. In addition, we used high-rate time-lapse photography to document calving events (one photograph per 10 s) and observe ice mélange activity (one photograph per 15 min).

We observed three modes of flow: (1) steady, coherent flow characterized by velocity and strain rate fields that vary smoothly throughout the fjord, (2) steady, incoherent flow in which the velocity

[1]Earth Science and Observation Center, Cooperative Institute for Research in Environmental Sciences, University of Colorado Boulder, Boulder, CO, USA. [2]Department of Physics, Emory University, Atlanta, GA, USA. [3]Department of Natural Sciences, University of Alaska Southeast, Juneau, AK, USA. [4]Geophysical Institute, University of Alaska Fairbanks, Fairbanks, AK, USA. ✉e-mail: ryan.cassotto@colorado.edu
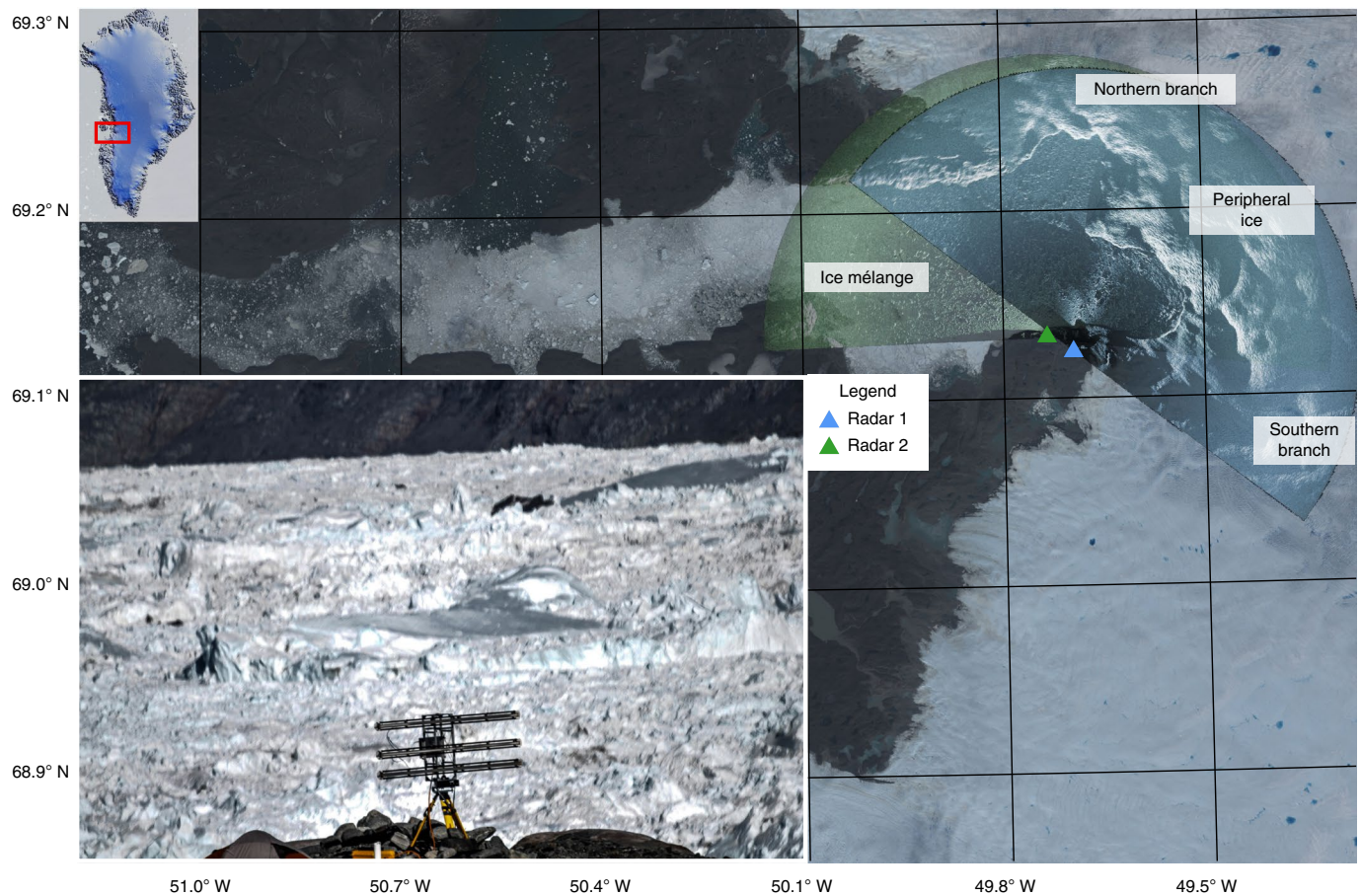
Fig. 1 | Jakobshavn Isbræ and proglacial ice mélange. The locations, viewing geometries and radar backscatter images from the pair of TRIs used in this study are shown superposed on a Landsat 8 image from June 2013. The reference hillshade image is created from NASA MEaSUREs Digital Elevation Model[49] data. Inset: photograph looking north across the fjord with TRI 2 in the foreground and large iceberg clasts within the ice mélange in the background. The Landsat 8 image was downloaded from the US Geological Survey's Earth Resources Observation and Science (EROS) Center.

field contains considerable variability at the grain scale and (3) rapid, irregular flow associated with dynamic jamming fronts propagating through the ice mélange, as previously described[20]. During steady, coherent flow, large regions of compressional and extensional strain rates appear in the velocity divergence fields ($\nabla \cdot \hat{U}$, Fig. 2b), yet ice mélange speeds ($|\hat{U}|$, Fig. 2a) are smooth because individual icebergs flow in concert with their neighbours, as evidenced by the velocity anomaly fields ($\hat{U} - \overline{U}$, Fig. 2c). By contrast, incoherent flow appears as highly localized patches of extensional and compressional strain rates that permeate throughout the ice mélange when individual icebergs begin to disaggregate and rotate randomly (Fig. 2d–f). Steady, coherent flow occurs during periods of terminus quiescence that spans hours to days and is therefore the predominant flow mechanism (Fig. 3a and Supplementary Videos 1 and 2), while incoherent flow is ephemeral and occurs immediately before and after calving events. The granular interactions that define these flow modes only become evident when observed using a pair of TRI instruments to produce 2D flow fields with approximate grain-scale spatial resolution (∼50 m) and fine-scale temporal sampling.

We observed 14 calving events overall, of which 7 were observed by both radars. All of the events can be classified into two distinct categories: those that caused widespread failure along the ice mélange shear margins and led to rapid kilometre-scale displacement of the entire ice mélange, and those that perturbed the ice mélange but did not result in large displacements (Supplementary Video 3). For all events, regardless of style, the velocity fields appear

smooth prior to the first visible evidence of an iceberg calving from the terminus. However, ∼1 h before a calving event, speeds increase (Figs. 2d and 3a) and the strain rate and velocity fields become increasingly speckled (Fig. 2e and Supplementary Video 2), indicating that small-scale particle rearrangements must be occurring (Fig. 2f). The loss of flow coherence preceding calving events is further illustrated by changes in the standard deviation in velocity, σ_U, sampled within ∼0.01-km² patches (Fig. 3), which increased simultaneously throughout the ice mélange (Fig. 3b–e). After calving, σ_U either remained highly variable and led to secondary calving events (Fig. 3b,d) or decreased over ∼1 h (Fig. 3c,e) as the ice mélange regained flow coherence. The size of the calving event and resultant displacement of icebergs within the ice mélange affected the recovery time, with larger events (2 August 8:08 and 10:25; 5 August 1:44, Supplementary Video 3) having longer recovery times (Fig. 3b,d). Overall, the peak in σ_U centred around calving events is remarkably symmetric and consistent across calving events, and the ∼1-h duration of flow decoherence is congruent with increased seismic activity from an earlier ice mélange study[10].

Local and global strain in a granular material

We interpret the loss of flow coherence as evidence of an increase in global strain in a highly jammed granular material. In the jammed state, granular flow is effectuated by local displacements of particles that are spatially heterogeneous, even for infinitesimally small strains. We observe that the global effective strain rate ($\dot{\epsilon}$), defined
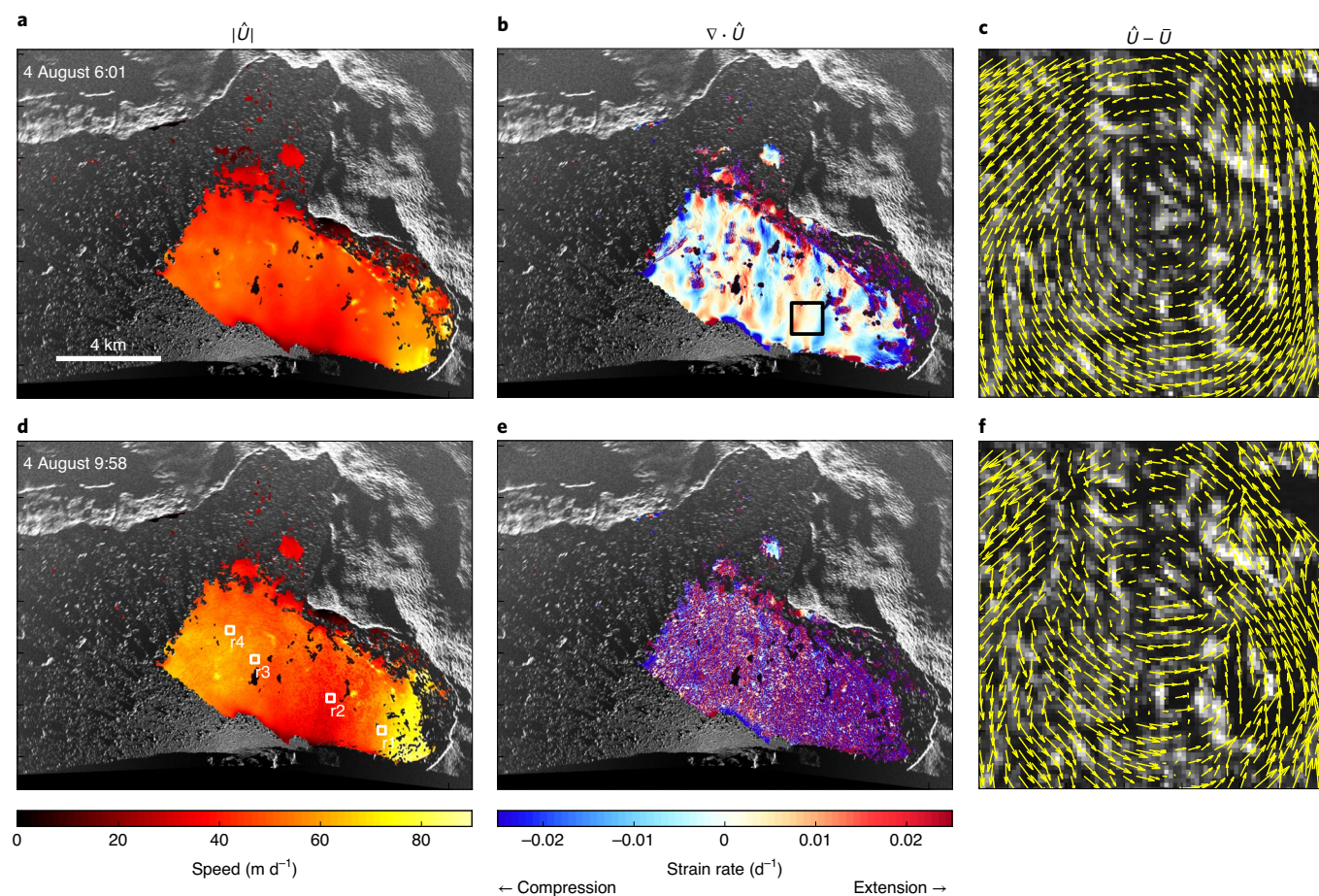
Fig. 2 | TRI-derived 2D velocity data products. a–c, Speeds (**a**), divergence in velocities (strain rates) (**b**) and velocity anomaly vectors for a subregion of ice mélange (black box in **b**) (**c**) during terminus quiescence. **d–f**, same as **a–c** but during a calving-imminent period. The four boxes in **d** (marked r1, r2, r3, r4) show the ~0.01-km² patches sampled in Fig. 3.

as the second invariant of the strain rate tensor averaged over the entire ice mélange, increases by ~0.1 d⁻¹ in the 1 h preceding a calving event (Fig. 3b–e), which corresponds to an overall strain of only 0.004.

To illustrate the connection between local and global strain, we simulated a collection of floating spherical particles in an open rectangular channel that is bounded by a fixed wall on one side (Fig. 4a). Under the influence of buoyant forces, the collection of particles experiences a quasi-static, uniaxial expansion along its length, L, to a final global strain of $\varepsilon = 0.001$. Figure 4b shows the magnitude of particle displacements for a simulated ice mélange of length $L = 8$ km. For an isotropic, continuum material, the displacement would vary linearly along the length. However, individual particles deviate substantially from this prediction, and velocity fields are spatially heterogeneous over a 1-km² area (Fig. 4c), in analogy with Fig. 2f. Localized regions of high strain appear where particles move in opposite directions, which we associate with soft spots[30], slip avalanches[31] or shear transformation zones[32], known to control plastic deformation in disordered materials.

A histogram of typical particle displacements with the linear portion removed shows the distribution has long, non-Gaussian tails with a standard deviation of 0.2 m (Fig. 4d). This implies that a tightly packed ice mélange undergoing uniaxial expansion with $\varepsilon = 0.001$ will have individual particles that experience ~0.2 m of random displacement, on average. This amount of displacement over a 1-h period corresponds to a standard deviation in velocity of 4.8 m d⁻¹, which is in good agreement with the data shown

in Fig. 3b–e. Thus, our model demonstrates that a subtle uniaxial expansion of the tightly packed ice mélange in the hour before calving leads to a loss of flow coherence through small displacements of individual icebergs.

## Flow decoherence precedes terminus activity

Together, our field observations and particle dynamics model indicate that increased global strain in jammed ice mélange is facilitated by flow decoherence that can be detected locally up to 1 h prior to calving events. These observations were only possible with data from a pair of terrestrial radar interferometers that have the necessary precision and range to measure millimetre-scale deformation at kilometre-scale distances over short time periods. The fact that calving during this period was always preceded by flow decoherence strongly implicates ice mélange as a mechanical inhibitor of calving. The transition from a tightly packed, jammed state to a dynamic unjammed state should be accompanied by a decrease in the mechanical force transmitted to the glacier terminus, thus promoting iceberg calving. The loss of flow coherence that we observe at Jakobshavn Isbræ is insufficient to cause widespread ice mélange dispersal; consequently, freshly calved icebergs quickly become incorporated into the ice mélange, suggesting that ice mélange may act as a stabilizing influence year-round. In fjord systems with smaller ice fluxes, oceanographic processes may dominate and therefore the loss of flow coherence during the first major calving event in spring may result in complete dispersal of ice mélange.
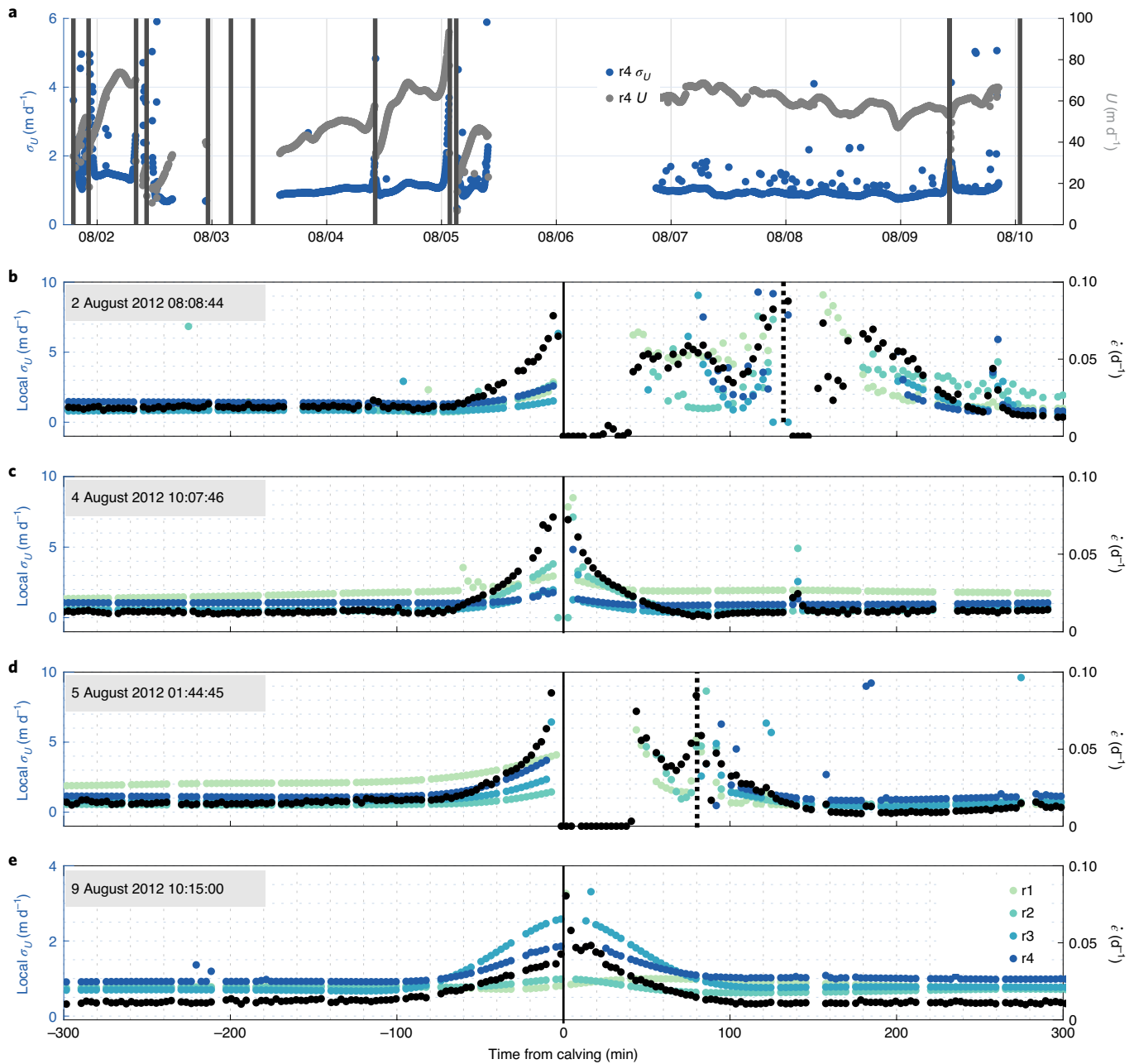
Fig. 3 | Variations in speed and bulk strain rate over time. a, Time-series of mean speeds (grey) and the standard deviation (σ_U, blue) of the speed sampled within r4, a single ~0.01-km² patch of ice mélange indicated in Fig. 2d. Calving events are indicated by grey vertical lines. **b–e**, σ_U (left axis) for four patches (r1–r4, shown in different colours) and global strain rates (right axis, $\dot{\varepsilon}$, black) averaged over the entire ice mélange and centred around calving for four different events. Dashed grey lines in **b** and **d** indicate the timing of secondary calving events.

We considered whether flow decoherence was simply a response to glacier dynamics and hypothesized that initial calving processes, such as crevasse opening and prolonged rotation of calving icebergs[33], promoted ice mélange expansion. TRI has millimetre-scale sensitivity[34] that can detect subtle surface changes associated with calving inception. We found no evidence of precursor motion along the glacier terminus in the derived data products of velocity (Extended Data Fig. 1) and strain rates[29], nor in the raw interferograms. Therefore, we conclude that flow decoherence in the ice mélange did not originate from glacier dynamic processes. Instead, calving ensued only after a small expansion of the ice mélange initiated a loss in flow coherence.

Jakobshavn Isbræ's ice mélange persistently flowed downfjord (Supplementary Video 4), in a westward direction, with the immediate proglacial ice mélange frequently accelerating prior to calving events (Extended Data Figs. 1, 2, 3 and 4). Several external forces can trigger an acceleration and downfjord expansion of the ice mélange, including katabatic winds[7,35]. An automatic weather station in the fjord indicates predominantly northerly (across-fjord) winds during our study[36], suggesting that wind shear was not a factor. The periodic downfjord accelerations of distal ice mélange (Supplementary Video 3) and increased speeds between tidal phases (Extended Data Figs. 2 and 3) suggest a tidal influence. Most calving events occurred during a spring tide (Extended Data Fig. 1), when the horizontal
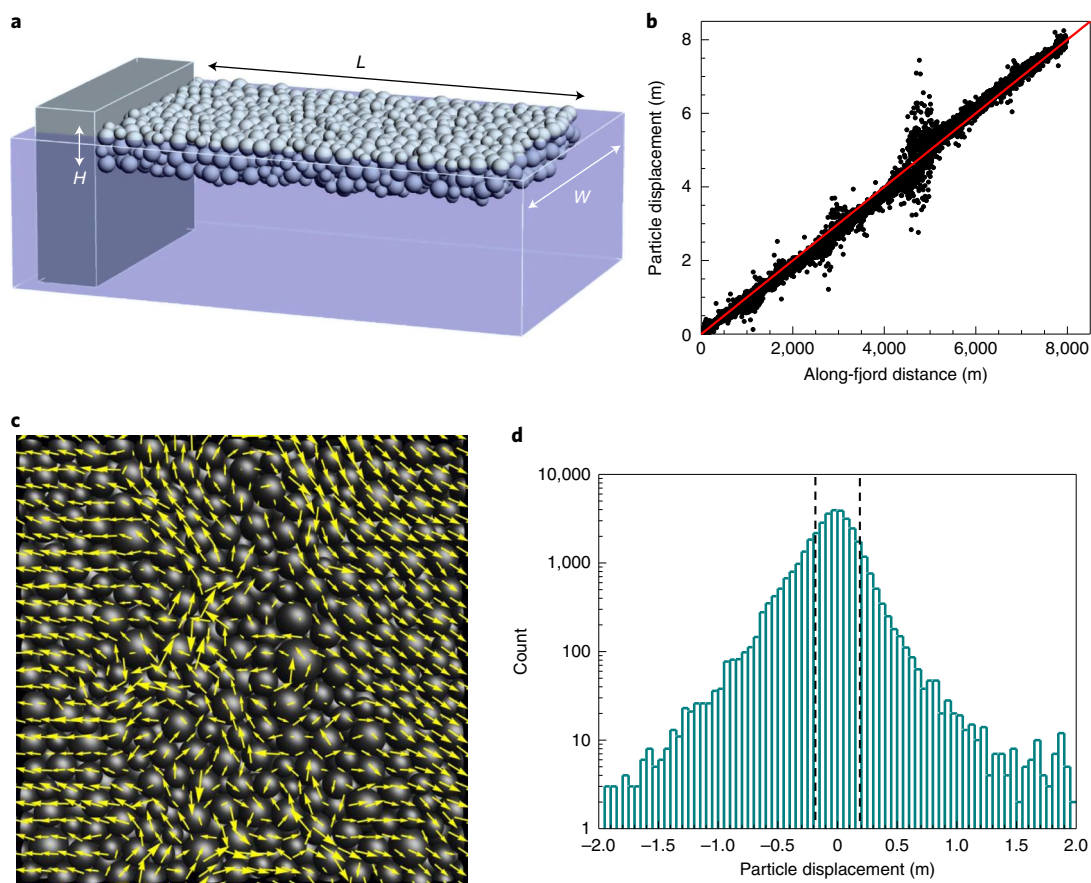
Fig. 4 | Particle dynamics model. a, Schematic of the polydisperse spherical, buoyant particles that quasi-statically expand against a fixed wall and the periodic boundary conditions along W; thus, $L \rightarrow L + \Delta L$. **b**, The results with 6,000 particles, with $L = 8,000$ m, $W = 1,000$ m and $H \approx 230$ m. For a global strain of $\varepsilon = 0.001$, the ice mélange expands ($\Delta L = 8$ m), allowing individual particle displacements to deviate from the continuum prediction (red line). **c**, Displacement vectors for a 1,000 m × 1,000 m section, showing local heterogeneities congruent with Fig. 2e. **d**, Particle displacements with global strain removed, showing a standard deviation of 0.2 m.

displacement of icebergs due to large ebb and flow current transitions is expected to be greatest. However, tidal oscillations also affect the basal water pressures that control subglacial discharge and fjord circulation[37], factors that enhance meltwater discharge during neap tides in other fjords[38]. Consequently, the downfjord expansion of the ice mélange via drag from submarine plumes cannot be ruled out, particularly during the late record. Therefore, although the downfjord expansion that initiated decoherence appears to be tidally modulated, complex feedbacks along the ice–ocean boundary obfuscate the true tidal mechanism.

Implications for glacier stability and granular failure
The response of tidewater glaciers to perturbations at their calving fronts is highly nonlinear and is sensitive to terminus location relative to the underlying bed topography[29,39,40]. Thus, by affecting the timing of iceberg calving over daily to monthly timescales, ice mélange can influence tidewater glacier stability and therefore ice-sheet mass balance over much longer time periods. Our findings imply that a comprehensive characterization of ice mélange rheology and iceberg calving is required in tidewater glacier models. Specifically, accounting for ice mélange with a seasonally varying resistive stress on the terminus[41,42] is insufficient, as it only affects stresses in the flow model and neglects the influence of ice mélange on the calving process along an already highly fractured glacier terminus. Our study demonstrates that ice mélange does, in fact, mechanically inhibit iceberg calving, even in the absence of a binding sea ice matrix. Many factors govern ice mélange stresses,

including iceberg production and retention, fjord geometry, sea ice availability, wind, tidal oscillations and subglacial discharge. A deeper understanding of these parameters and how they affect stress transmission within the ice mélange are necessary before ice mélange can be properly incorporated into ice-sheet models.

Finally, our application of TRI to study the transitions between incoherent and coherent flow demonstrates an important advance for granular mechanics in general. Predicting impending failure in disordered systems is a principal goal in many fields, ranging from earthquake detection[43,44] to glassy[45], granular[46,47] and mechanical metamaterials[48]. Particle and bond-level information plays a crucial role in predicting failure, which until now has remained unavailable for complex geophysical systems. In flowing granular materials, machine learning techniques and acoustic emissions analyses demonstrate precursors to failure, although real-time detection remains an elusive goal. Thus, our study represents an important first step towards real-time detection of failure in geophysical granular flows such as sea ice, rock and snow avalanches, the liquefaction of granular soils, and debris flows.

Online content
Any methods, additional references, Nature Research reporting summaries, source data, extended data, supplementary information, acknowledgements, peer review information; details of author contributions and competing interests; and statements of data and code availability are available at https://doi.org/10.1038/s41561-021-00754-9.

References

1. Amundson, J. M. et al. Ice mélange dynamics and implications for terminus stability, Jakobshavn Isbræ, Greenland. *J. Geophys. Res. Earth Surf.* **115**, F01005 (2010).
2. Enderlin, E. M., Hamilton, G. S., Straneo, F. & Sutherland, D. A. Iceberg meltwater fluxes dominate the freshwater budget in Greenland's iceberg-congested glacial fjords. *Geophys. Res. Lett.* **43**, 11287–11294 (2016).
3. Moon, T. et al. Subsurface iceberg melt key to Greenland fjord freshwater budget. *Nat. Geosci.* **11**, 49–54 (2018).
4. Martin, T., Tsamados, M., Schroeder, D. & Feltham, D. L. The impact of variable sea ice roughness on changes in Arctic Ocean surface stress: a model study. *J. Geophys. Res. Oceans* **121**, 1931–1952 (2016).
5. Hewitt, I. J. Subglacial plumes. *Annu. Rev. Fluid Mech.* **52**, 145–169 (2020).
6. Davison, B. J., Cowton, T. R., Cottier, F. R. & Sole, A. J. Iceberg melting substantially modifies oceanic heat flux towards a major Greenlandic tidewater glacier. *Nat. Commun.* **11**, 5983 (2020).
7. Cassotto, R., Fahnestock, M., Amundson, J. M., Truffer, M. & Joughin, I. Seasonal and interannual variations in ice mélange and its impact on terminus stability, Jakobshavn Isbræ, Greenland. *J. Glaciol.* **61**, 76–88 (2015).
8. Joughin, I., Shean, D. E., Smith, B. E. & Floricioiu, D. A decade of variability on Jakobshavn Isbræ: ocean temperatures pace speed through influence on mélange rigidity. *Cryosphere* **14**, 211–227 (2020).
9. Ekstrom, G., Nettles, M. & Abers, G. A. Glacial earthquakes. *Science* **302**, 622–624 (2003).
10. Amundson, J. M. et al. Glacier, fjord and seismic response to recent large calving events, Jakobshavn Isbræ, Greenland. *Geophys. Res. Lett.* **35**, L22501 (2008).
11. Nettles, M. et al. Step-wise changes in glacier flow speed coincide with calving and glacial earthquakes at Helheim Glacier, Greenland. *Geophys. Res. Lett.* **35**, L24503 (2008).
12. Murray, T. et al. Reverse glacier motion during iceberg calving and the cause of glacial earthquakes. *Science* **349**, 305–308 (2015).
13. Cates, M. E., Wittmer, J. P., Bouchaud, J. P. & Claudin, P. Jamming, force chains and fragile matter. *Phys. Rev. Lett.* **81**, 1841–1844 (1998).
14. Liu, A. J. & Nagel, S. R. The jamming transition and the marginally jammed solid. *Annu. Rev. Condens. Matter Phys.* **1**, 347–369 (2010).
15. Behringer, R. P. & Chakraborty, B. The physics of jamming for granular materials: a review. *Rep. Prog. Phys.* **82**, 012601 (2018).
16. Burton, J. C., Amundson, J. M., Cassotto, R., Kuo, C.-C. & Dennin, M. Quantifying flow and stress in ice mélange, the world's largest granular material. *Proc. Natl Acad. Sci. USA* **115**, 5105–5110 (2018).
17. Robel, A. A. Thinning sea ice weakens buttressing force of iceberg mélange and promotes calving. *Nat. Commun.* **8**, 14596 (2017).
18. Amundson, J. M. & Burton, J. C. Quasi-static granular flow of ice mélange. *J. Geophys. Res. Earth Surf.* **123**, 2243–2257 (2018).
19. Waitukaitis, S. R., Roth, L. K., Vitelli, V. & Jaeger, H. M. Dynamic jamming fronts. *Europhys. Lett.* **102**, 44001 (2013).
20. Peters, I. R. et al. Dynamic jamming of iceberg-choked fjords. *Geophys. Res. Lett.* **42**, 1122–1129 (2015).
21. Jaeger, H. M. & Nagel, S. R. Physics of the granular state. *Science* **255**, 1523–1532 (1992).
22. Bi, D., Zhang, J., Chakraborty, B. & Behringer, R. P. Jamming by shear. *Nature* **480**, 355–358 (2011).
23. Thomas, A. L., Tang, Z., Daniels, K. E. & Vriend, N. M. Force fluctuations at the transition from quasi-static to inertial granular flow. *Soft Matter* **15**, 8532–8542 (2019).
24. Ferdowsi, B., Ortiz, C. P., Houssais, M. & Jerolmack, D. J. River-bed armouring as a granular segregation phenomenon. *Nat. Commun.* **8**, 1363 (2017).
25. King, M. D. et al. Seasonal to decadal variability in ice discharge from the Greenland Ice Sheet. *Cryosphere* **12**, 3813–3825 (2018).
26. Xie, S., Dixon, T. H., Holland, D. M., Voytenko, D. & Vaňková, I. Rapid iceberg calving following removal of tightly packed pro-glacial mélange. *Nat. Commun.* **10**, 3250 (2019).
27. Nghiem, S. V. et al. The extreme melt across the Greenland Ice Sheet in 2012. *Geophys. Res. Lett.* https://doi.org/10.1029/2012GL053611 (2012).
28. Voytenko, D. et al. Acquisition of a 3-min, two-dimensional glacier velocity field with terrestrial radar interferometry. *J. Glaciol.* **63**, 629–636 (2017).
29. Cassotto, R. et al. Non-linear glacier response to calving events, Jakobshavn Isbræ, Greenland. *J. Glaciol.* **65**, 39–54 (2018).
30. Manning, M. L. & Liu, A. J. Vibrational modes identify soft spots in a sheared disordered packing. *Phys. Rev. Lett.* **107**, 108302 (2011).
31. Denisov, D. V., Lörincz, K. A., Uhl, J. T., Dahmen, K. A. & Schall, P. Universality of slip avalanches in flowing granular matter. *Nat. Commun.* **7**, 10641 (2016).
32. Langer, J. S. Shear-transformation-zone theory of yielding in athermal amorphous materials. *Phys. Rev. E* **92**, 012318 (2015).
33. Murray, T. et al. Dynamics of glacier calving at the ungrounded margin of Helheim Glacier, southeast Greenland. *J. Geophys. Res. Earth Surf.* **120**, 964–982 (2015).
34. Werner, C., Strozzi, T., Wiesmann, A. & Wegmuller, U. A real-aperture radar for ground-based differential interferometry. In *Proc. 2008 IEEE International Geoscience and Remote Sensing Symposium* III-210–III-213 (IEEE, 2008).
35. Walter, J. I. et al. Oceanic mechanical forcing of a marine-terminating Greenland glacier. *Ann. Glaciol.* **53**, 181–192 (2012).
36. Holland, D. M. *Air Temperature, Relative Humidity, and Others Collected from Automatic Weather Station Installed on Rock Outcrop in Jakobshavn Glacier Ice Front from 2007-10-13 to 2016-02-14 (NCEI Accession 0148760)* (NCEI, 2016).
37. Motyka, R. J., Dryer, W. P., Amundson, J., Truffer, M. & Fahnestock, M. Rapid submarine melting driven by subglacial discharge, LeConte Glacier, Alaska. *Geophys. Res. Lett.* **40**, 5153–5158 (2013).
38. Washam, P., Nicholls, K. W., Munchow, A. & Padman, L. Summer surface melt thins Petermann Gletscher Ice Shelf by enhancing channelized basal melt. *J. Glaciol.* **65**, 662–674 (2019).
39. Carr, J. R. et al. Basal topographic controls on rapid retreat of Humboldt Glacier, northern Greenland. *J. Glaciol.* **61**, 137–150 (2015).
40. Åkesson, H., Nisancioglu, K. H. & Nick, F. M. Impact of fjord geometry on grounding line stability. *Front. Earth Sci.* **6**, 71 (2018).
41. Todd, J. & Christoffersen, P. Are seasonal calving dynamics forced by buttressing from ice mélange or undercutting by melting? Outcomes from full-Stokes simulations of Store Glacier, West Greenland. *Cryosphere* **8**, 2353–2365 (2014).
42. Krug, J., Durand, G., Gagliardini, O. & Weiss, J. Modelling the impact of submarine frontal melting and ice mélange on glacier dynamics. *Cryosphere* **9**, 989–1003 (2015).
43. Johnson, P. A. & Jia, X. Nonlinear dynamics, granular media and dynamic earthquake triggering. *Nature* **437**, 871–874 (2005).
44. Rouet-Leduc, B. et al. Machine learning predicts laboratory earthquakes. *Geophys. Res. Lett.* **44**, 9276–9282 (2017).
45. Schoenholz, S. S., Cubuk, E. D., Sussman, D. M., Kaxiras, E. & Liu, A. J. A structural approach to relaxation in glassy liquids. *Nat. Phys.* **12**, 469–471 (2016).
46. Berthier, E., Porter, M. A. & Daniels, K. E. Forecasting failure locations in 2-dimensional disordered lattices. *Proc. Natl Acad. Sci. USA* **116**, 16742–16749 (2019).
47. Michlmayr, G., Cohen, D. & Or, D. Shear-induced force fluctuations and acoustic emissions in granular material. *J. Geophys. Res.* **118**, 6086–6098 (2013).
48. Driscoll, M. M. et al. The role of rigidity in controlling material failure. *Proc. Natl Acad. Sci. USA* **113**, 10813–10817 (2016).
49. Howat, I. M., Negrete, A. & Smith, B. E. *MEaSUREs Greenland Ice Sheet Mapping Project (GIMP) Digital Elevation Model. NASA National Snow and Ice Data Center Distributed Active Archive Center* (NSIDC, 2015); https://doi.org/10.5067/NV34YUIXLP9W

Methods

Radar acquisitions and processing. The TRI scans were acquired in 2012 using a pair of Gamma Remote Sensing ground portable radar interferometers (GPRI-II). Both radars were deployed along the southern fjord wall and separated by 1.9 km to provide favourable incidence angles (Fig. 1). The radars scanned the terminus and ice mélange every 3 min from 1 to 9 August, with limited breaks. Each instrument used a 180° scan in azimuth with a 16-km-range radius, and scan times were synchronized using GPS time codes.

Data from each radar were processed independently and then combined to create 2D velocity fields following Voytenko and colleagues[28]. Raw data were processed to single-look complex images, multi-looked by 15 in range (to an effective range resolution of 11.25 m) and used to create 3-min displacement interferograms. The interferograms were then filtered using an adaptive filter[50] and unwrapped (converted from relative phase measurements to absolute phase displacements) using a minimum cost flow (mcf) technique[51]. The mcf method unwrapped the majority of interferograms in the record in a clean and consistent manner; however, unwrapping errors of 1–2 integer cycle slips still occurred. Left unaccounted for, these phase jumps would produce erroneous step changes in speed of 4.08–8.16 m d^{-1}. To correct this, we applied a smoothing spline through time to each pixel in the unwrapped interferograms. Spline fits were calculated over the shorter of daily intervals or inter-calving periods. This approach produces smoothly varying velocity fields free of unwrapping errors at the expense of obscuring transient signals due to rolling icebergs or calving events from the northern terminus.

After correcting for phase unwrapping errors, we converted displacements to line-of-sight (LOS) speeds. A total of 2,397 interferogram pairs were then used to create 2D velocity fields following the methods of Voytenko and colleagues[28]. The method produces northing and easting velocity components that were used to calculate speeds in the direction of flow (that is, non-LOS). The accuracy of these velocity fields decreases when the radars have similar look angles. This biased speeds in pixels on the outside of the radar locations high (that is, east of radar 1 and west of radar 2). To account for this geometric distortion, we scaled the velocity fields by the ratio of image correlated speeds against the phase-based measurements. The image correlation was performed on the radar backscatter images that were not affected by LOS geometry issues; however, the technique has a lower sensitivity to motion and thus cannot be performed over short intervals. We used PyCORR (Python image Correlation package[52]) to derive velocities from backscatter image pairs acquired 24 h apart, with subsequent pairs offset by 1 h. In total, 50 image velocity pairs were calculated between 6 August 20:51 and 8 August 19:21, a period of terminus quiescence and continuous radar measurements. We averaged all 50 fields to produce maps of mean velocities in each direction (V_x, V_y) and applied a 39×39-pixel (585 m×585 m) square Gaussian low-pass filter to smooth the results. Next, we calculated the mean velocity fields in the phase-derived record using 1,109 3-min fields acquired over the same time period. We divided the mean PyCORR velocities by the mean phase-based values to produce a scaling map, and then multiplied the entire record of 2,397 phase-derived 2D velocity fields by this map. This resulted in a dense record of 2D speeds with high temporal resolution (3 min) to accurately measure iceberg motion within the ice mélange with minimal geometric distortion due to similarities in radar LOS viewing angles.

To evaluate errors in the 2D ice mélange speeds, we compared the final phase-derived products against PyCORR-derived speeds over the same 47-h period of quiescent flow (Extended Data Fig. 5). The biggest differences occurred in the shear margins, where differences between the two methods typically exceeded 10 m d^{-1} (Extended Data Fig. 5c). Shear margins are challenging for image-to-image correlation and also lie outside the main ice mélange 'plug', the main region of interest for our study. Therefore, we excluded these outliers in our error analysis and calculated the mean offsets, which resulted in an offset of −1.7 m d^{-1} in the phase-derived speeds with a standard deviation of 2.8 m d^{-1} (phase-based minus PyCORR). We adopted the latter as a conservative error estimate in the 2D derived speeds.

We derived strain rates by calculating the gradients in velocity for each component. The two normal components were summed to calculate the divergence of the velocity field ($\nabla \cdot \hat{U}$; Fig. 2). All four components ($\dot{\epsilon}_{xx}$, $\dot{\epsilon}_{xy}$, $\dot{\epsilon}_{yx}$, $\dot{\epsilon}_{yy}$) were used to calculate the 2D effective strain rate (second invariant of the strain rate tensor) in each pixel, and then integrated over the entire ice mélange and divided by the number of valid data points to produce an estimate of the global strain rates in the ice mélange at each interval (Fig. 3b–e).

Model. We used a custom particle dynamics code for the simulations. In each simulation, the particle radii (R) were drawn from a Gaussian distribution with mean of 25 m and standard deviation of 10 m, with particle sizes less than 25 m and greater than 200 m removed. Each particle experienced a buoyant force due to the amount of submerged volume below the vertical position $z=0$ m (the fluid surface). The fluid density was 1,027 kg m^{-3} and the particle density was 900 kg m^{-3}. The particles also experienced a harmonic, repulsive force (proportional to the amount of geometric overlap between their surfaces, equal to $k(r_{ij} - R_i - R_j)$), where $k=2$ N m^{-1} is the stiffness of the iceberg particles (~20 times larger than the load on the terminus), r_{ij} is the distance between their centres and R_i and R_j are their radii. Tangential friction was not included in the simulation. Particles also experienced an identical repulsive force from geometric overlap with the channel walls. Initially, $N=6,000$ spherical particles were placed at random in a channel of length $L=8,000$ m, width $W=1,000$ m and vertical depth=1,000 m below the fluid surface. Solid walls were imposed at $x=0$ and $x=L$, and periodic boundary conditions were imposed at $y=-W/2$ and $y=W/2$. The potential energy of the system was then quenched to the nearest local minimum using the FIRE algorithm[53], which resulted in a buoyant layer of particles near the fluid surface with thickness $H \approx 230$ m. The system was then quasi-statically strained by allowing one wall of the channel to expand in length by $\Delta L=8$ m in 300 equal steps, thus reaching a final uniaxial strain of $\varepsilon=0.001$. The potential energy was minimized at each step to maintain equilibrium throughout the expansion.

Data availability
The TRI-derived 2D velocity dataset generated and analysed during the current study will be available at the National Snow and Ice Data Center (https://nsidc.org; https://doi.org/10.5067/FKPL8IY02XWS).

References
50. Goldstein, R. M. & Werner, C. L. Radar interferogram filtering for geophysical applications. *Geophys. Res. Lett.* **25**, 4035–4038 (1998).
51. Goldstein, R. M., Zebker, H. A. & Werner, C. L. Satellite radar interferometry: two-dimensional phase unwrapping. *Radio Sci.* **23**, 713–720 (1988).
52. Fahnestock, M. et al. Rapid large-area mapping of ice flow using Landsat 8. *Remote Sens. Environ.* **185**, 84–94 (2016).
53. Bitzek, E., Koskinen, P., Gähler, F., Moseler, M. & Gumbsch, P. Structural relaxation made simple. *Phys. Rev. Lett.* **97**, 170201 (2006).

Author contributions
R.K.C., J.M.A., M.A.F. and M.T. collected the TRI data. R.K.C. processed and analysed the data with input from all collaborators. J.C.B. created and completed the modelling component. R.K.C., J.C.B. and J.M.A. authored the manuscript with input from M.A.F. and M.T.

Competing interests
The authors declare no competing interests.

Additional information
Extended data is available for this paper at https://doi.org/10.1038/s41561-021-00754-9.

Supplementary information The online version contains supplementary material available at https://doi.org/10.1038/s41561-021-00754-9.

Correspondence and requests for materials should be addressed to R.K.C.

Peer review information *Nature Geoscience* thanks Douglas Jerolmack and the other, anonymous, reviewer(s) for their contribution to the peer review of this work. Primary Handling Editor: James Super.

**Reprints and permissions information** is available at www.nature.com/reprints.
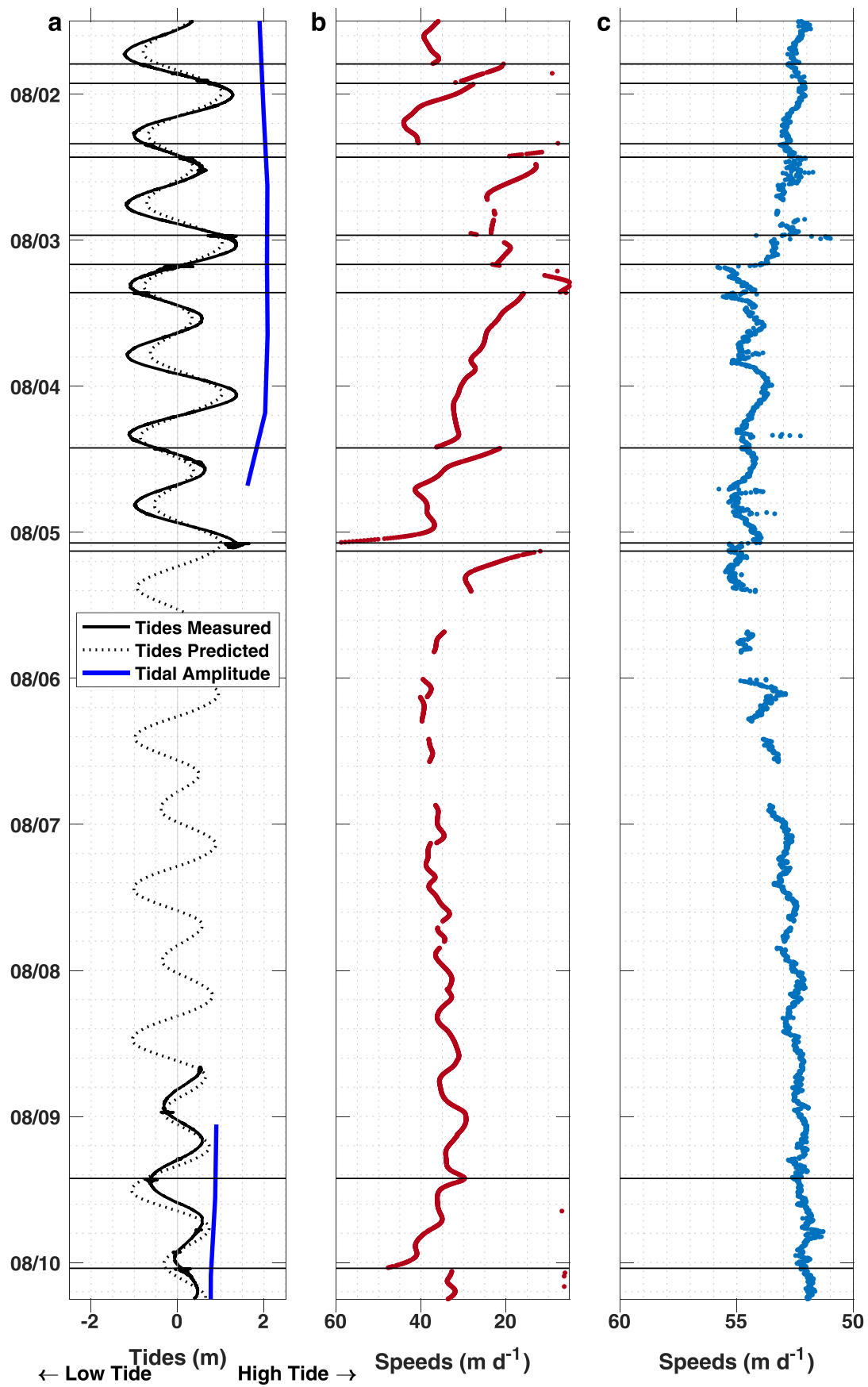
Extended Data Fig. 1 | See next page for caption.

Extended Data Fig. 1 | The relationship between iceberg calving, ocean tides, line-of-sight ice mélange speeds, and glacier speeds. The relationship between iceberg calving (black horizontal lines), (a) ocean tides, (b) line-of-sight ice mélange speeds and (c) glacier speeds with time ascending down along the y-axis in all panels. Most of the calving occurred during a spring tide when tidal amplitudes (mean difference between two high and two low tides each day) were high. Mélange speeds were similar in magnitude but more variable than glacier speeds, indicating proglacial mechanisms affect ice mélange flow. For nearly all calving events, an increase in mélange speeds occurred without coincident increase in glacier speeds; the sole exception was Aug 9 when a small calving event was precipitated by a partial loss of mélange flow coherence located downfjord of the sampled time-series.
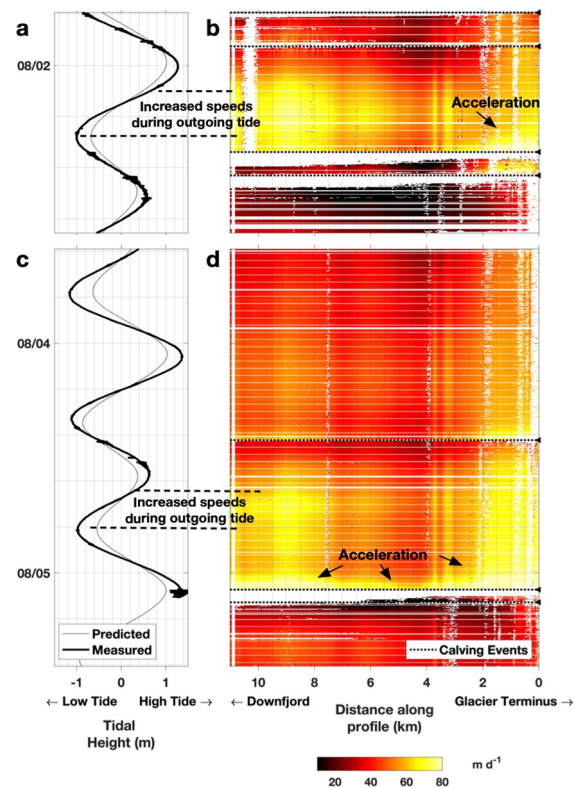
Extended Data Fig. 2 | Tidal oscillations in mélange flow for two different time periods in the early record. (a) Tidal height measured ~5 km from the calving front and (b) Mélange 2D-derived speeds sampled along a centerline profile between Aug 1 19:02 and Aug 2 15:25. (c,d) same as (a,b) but for Aug 3 14:13 – Aug 5 9:43. Time ascends downward along the y-axis for all plots. The location of the profiles is shown in Extended Data Fig. 4.
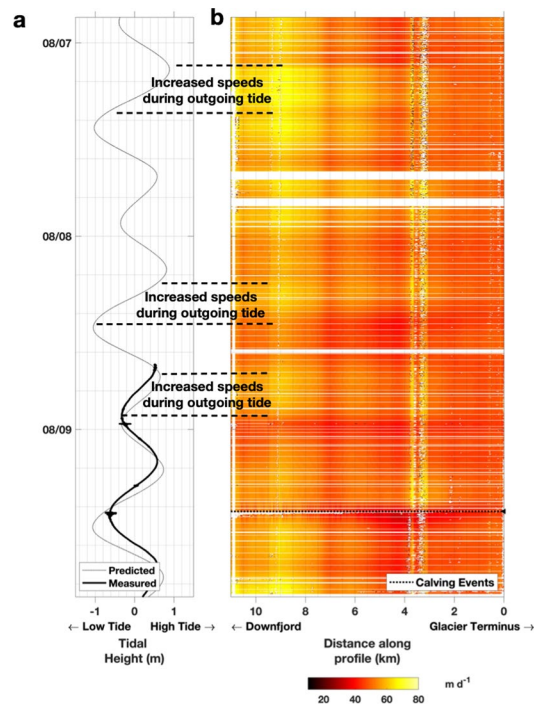
Extended Data Fig. 3 | Tidal oscillations in mélange flow for the time period Aug 6 20:52 – Aug 9 20:28. (a) Tidal height measured ~5 km from the calving front. (b) Mélange 2D-derived speeds sampled along a center line profile shown in Extended Data Fig. 4. Time ascends downward along the y-axis for both plots.
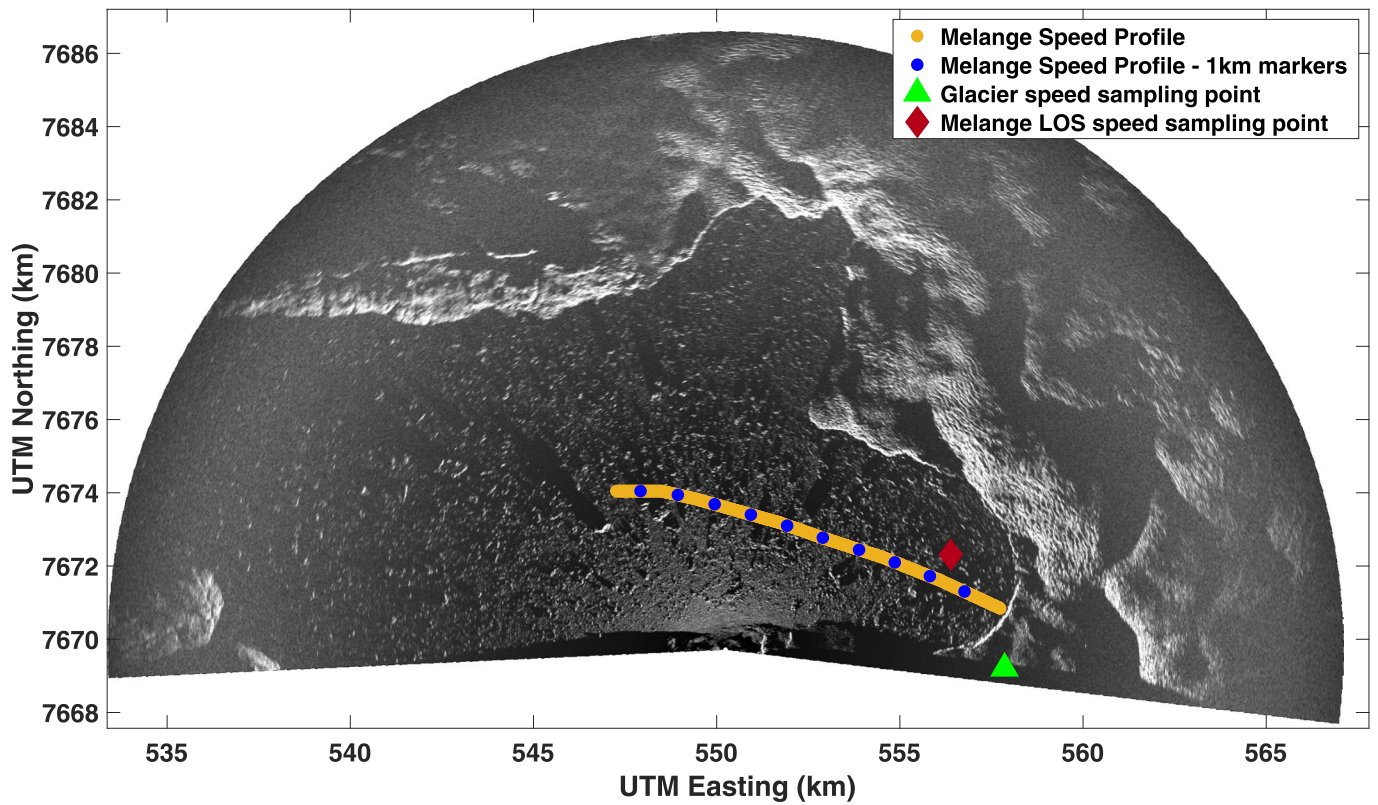
Extended Data Fig. 4 | TRI backscatter reference image. TRI backscatter reference image showing the locations of the mélange 1D line-of-sight (maroon) and glacier speed (green; from Cassotto et al.[29]) time-series shown in Extended Data Fig. 1. The location of a center profile (orange) used to sample mélange 2D speeds in Extended Data Figs. 2 and 3 is also shown; blue points indicate 1-km distances along the profile.
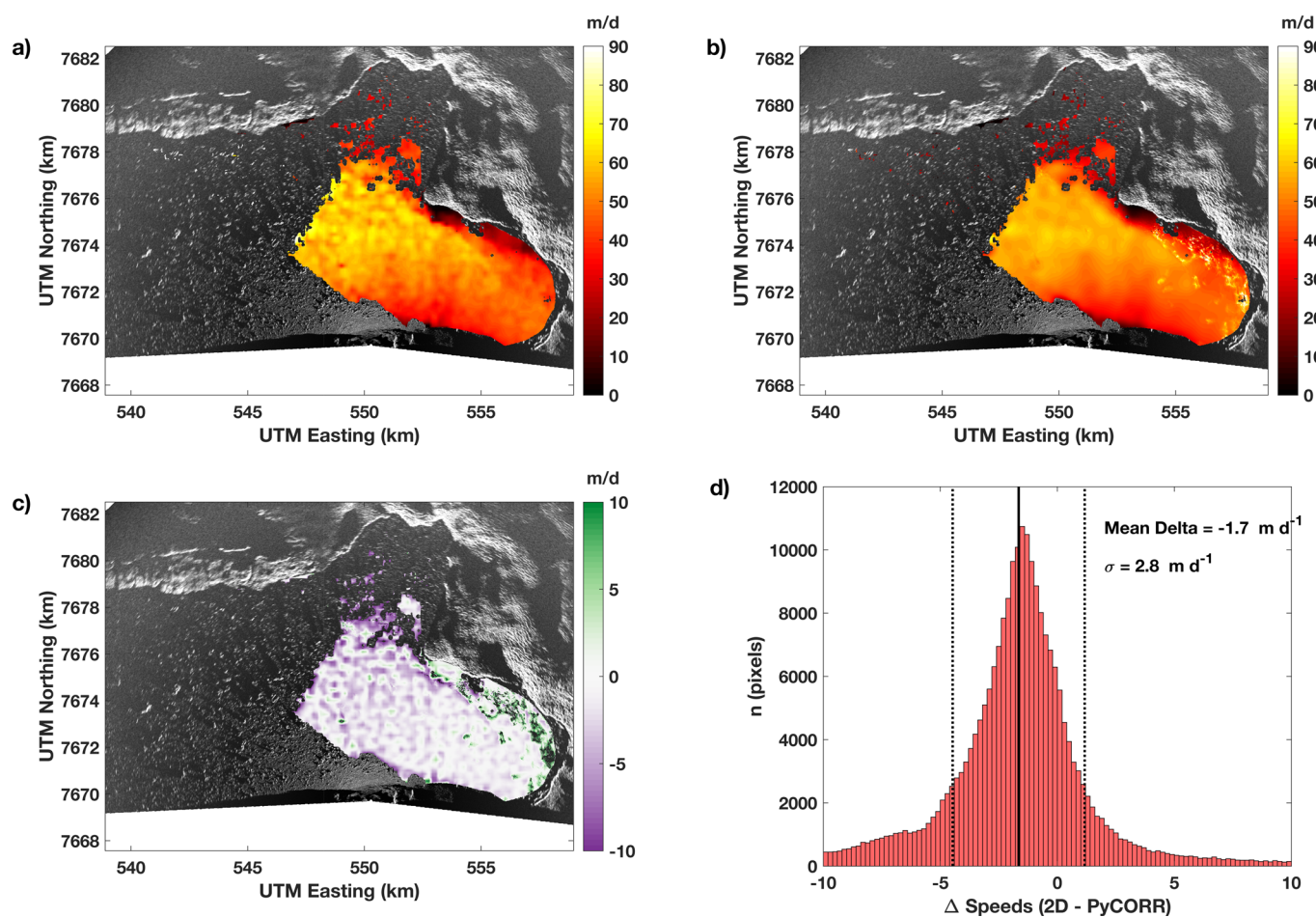
Extended Data Fig. 5 | Error Analysis. Mean speeds between Aug 6 20:51 and Aug 8 19:21, 2012 derived from (a) PyCORR and (b) phase-based values. The difference between each method (phase-based minus PyCORR) shown in (c) map view and as a (d) histogram. The phase-based values are 1.7 m d⁻¹ lower than PyCORR derived values with a standard deviation of 2.8 m d⁻¹; we adopt the latter as the error in phase derived velocity fields.